A grating-bicoupled plasma-wave photomixer with resonant-cavity enhanced structure

Taiichi Otsuji, Mitsuhiro Hanabe, and Takuya Nishimura

Research Institute of Electrical Communication, Tohoku University,
2-1-1 Katahira, Aoba-ku, Sendai 980-8577, Japan
otsuji@riec.tohoku.ac.jp, hanabe@riec.tohoku.ac.jp, nishimura@riec.tohoku.ac.jp

Eiichi Sano

Research Center for Integrated Quantum Electronics, Hokkaido University,
Nishi 8, Kita 13-Jo, Kita-ku, Sapporo, Hokkaido, 060-8628, Japan
esano@rciqe.hokudai.ac.jp

Abstract: A novel terahertz plasma-wave photomixer that can improve the conversion gain and terahertz radiation power is proposed and evaluated. The photomixer is based on a high-electron mobility transistor and incorporates doubly interdigitated grating strips for the gate electrodes that periodically localize the 2D plasmons in 100-nm regions with a micron-order interval. A vertical cavity structure is formed in between the top metal grating and a terahertz mirror placed at the backside. The device features electronic tuning of plasmon characteristic frequencies, providing continuously-tunable operation below 1 THz to beyond 10 THz. Frequency-dependent finite-differential time-domain analysis demonstrates that the grating-bicoupled plasmonic structure acts as a broadband terahertz photomixer and antenna and that the vertical cavity structure effectively enhances the conversion gain and radiation power.

©2005 Optical Society of America

OCIS codes: (230.5590) Quantum-well devices; (230.6080) Sources; (240.6680) Surface plasmons

---

References and links

1. M. Dyakonov and M. Shur, "Shallow water analogy for a ballistic field effect transistor: new mechanism of plasma wave generation by dc current," Phys. Rev. Lett. **71**, 2465-2468 (1993).
2. M. Dyakonov and M. Shur, "Detection, mixing, and frequency multiplication of terahertz radiation by two-dimensional electronic fluid," IEEE Trans. Electron Devices **43**, 380-387 (1996).
3. A. V. Chaplik, "Possible crystallization of charge carriers in low-density inversion layers," Sov. Phys. JETP **35**, 395-398 (1972).
4. M. Nakayama, "Theory of surface waves coupled to surface carriers," J. Phys. Soc. Jap. **36**, 393-398 (1974).
5. F. J. Crowne, "Contact boundary conditions and the Dyakonov-Shur instability in high electron mobility transistors," J. Appl. Phys. **82**, 1242-1254 (1997).
6. S. A. Mikhailov, "Plasma instability and amplification of electromagnetic waves in low-dimensional electron systems," Phys. Rev. B **58**, 1517-1532 (1998).
7. M. V. Cheremisin, M. I. Dyakonov, M. S. Shur, and G. Samsonidze, "Influence of electron scattering on current instability in field effect transistors," Solid-State Electron. **42**, 1737-1742 (1998).
8. F. J. Crowne, "Dyakonov-Shur plasma excitations in the channel of a real high-electron mobility transistor," J. Appl. Phys. **87**, 8056-8063 (2000).
9. T. Otsuji, S. Nakae, and H. Kitamura, "Numerical analysis for resonance properties of plasma-wave field-effect transistors and their terahertz applications to smart photonic network systems," IEICE Trans. Electron. **E84-C**, 1470-1476 (2001).
10. V. Ryzhii and M. Shur, "Analysis of tunneling-injection transit-time effects and self-excitation of terahertz plasma oscillations in high-electron-mobility transistors," Jpn. J. Appl. Phys. **41**, L922-L924 (2002).
11. V. Ryzhii, I. Khmyrova, and M. Shur, "Terahertz photomixing in quantum well structures using resonant excitation of plasma oscillations," J. Appl. Phys. **91**, 1875-1881(2002).

12. V. Ryzhii, I. Kymyrova, A. Sato, P. O. Vaccaro, T. Aida, and M. Shur, "Plasma mechanism of terahertz photomixing in high-electron mobilitytransistor under interband photoexcitation," J. Appl. Phys. **92**, 5756-5760 (2002).
13. A. Satou, V. Ryzhii, I. Khmyrova, M. Ryzhii, and M. S. Shur, "Characteristics of a terahertz photomixer based on a high-electron mobility transistor structure with optical input through the ungated regions," J. Appl. Phys. **95**, 2084-2089 (2004).
14. S. J. Allen, Jr., D. C. Tsui, and R. A. Logan, "Observation of the two-dimensional plasmon in silicon inversion layers," Phys. Rev. Lett. **38**, 980-983 (1977).
15. D. C. Tsui, E. Gornik, and R. A. Logan, "Far infrared emission from plasma oscillations of Si inversion layers," Solid State Comm. **35**, 875-877 (1980).
16. R. J. Wilkinson, C. D. Ager, T. Duffield, H. P. Hughes, D. G. Hasko, H. Armed, J. E. F. Frost, D. C. Peacock, D. A. Ritchie, A. C. Jones, C. R. Whitehouse, and N. Apsley, "Plasmon excitation and self-coupling in a bi-periodically modulated two-dimensional electron gas," J. Appl. Phys. **71**, 6049-6061 (1992).
17. K. Hirakawa, K. Yamanaka, M. Grayson, and D. C. Tsui, "Far-infrared emission spectroscopy of hot two-dimensional plasmons in $Al_{0.3}Ga_{0.7}As/GaAs$ heterojunctions," Appl. Phys. Lett. **67**, 2326-2328 (1995).
18. J.-Q. Lü, M. Shur, J. L. Hesler, L. Sun, and R. Weikle, "Terahertz detector utilizing two-dimensional electronic fluid," IEEE Electron Device Lett. **19**, 373-375 (1998).
19. N. Sekine, K. Yamanaka, K. Hirakawa, M. Voseburger, P. Haring-Bolivar, and H. Kurz, "Observation of terahertz radiation from higher-order two-dimensional plasmon modes in GaAs/AlGaAs single quantum wells," Appl. Phys. Lett. **74**, 1006-1008 (1999).
20. M. Shur and J.-Q. Lü, "Terahertz sources and detectors using two-dimensional electronic fluid in high-electron mobility transistors," IEEE Trans. Microwave Theory and Tech. **48**, 750-756 (2000).
21. T. Otsuji, Y. Kanamaru, H. Kitamura, and S. Nakae, "Terahertz plasma-wave excitation in 80-nm gate-length GaAs MESFET by photomixing long-wavelength CW laser sources," in *Digest of the 59th Annual Device Research Conference*, (Nortre Dame, Indiana, 2001), pp. 97-98.
22. W. Knap, Y. Deng, S. Rumyantsev, and M. S. Shur, "Resonant detection of subterahertz and terahertz radiation by plasma waves in submicron field-effect transistors," Appl. Phys. Lett., **81**, 4637-4639 (2002).
23. X. G. Peralta, S. J. Allen, M. C. Wanke, N. E. Harff, J. A. Simmons, M. P. Lilly, J. L. Reno, P. J. Burke, and J. P. Eisenstein, "Terahertz photoconductivity and plasmon modes in double-quantum-well field-effect transistors," Appl. Phys. Lett. **81**, 1627-1629 (2002).
24. T. Otsuji, Y. Kanamaru, H. Kitamura, M. Matsuoka, and O. Ogawara, "Effects of heterostructure 2D-electron confinement on the tunability of resonant frequencies of terahertz plasma-wave transistors," IEICE Trans. Electron. **E86-C**, 1985-1993 (2003).
25. W. Knap. J. Lusakowski, T. Parenty, S. Bollaert, A. Cappy, V. V. Popov, and M. Shur, "Terahertz emission by plasma waves in 60 nm gate high electron mobility transistors," Appl. Phys. Lett. **84**, 2331-2333 (2004).
26. D. Seliuta, E. Sirmulis, V. Tamosiunas, S. Balakauskas, S. Asmontas, A. Suziedelis, J. Gradauskas, G. Valusis, A. Lisauskas, H. G. Roskos, and K. Kohler, "Detection of terahertz/sub-terahertz radiation by asymmetrically-shaped 2DEG layers," Electron. Lett. **40**, 631-632 (2004).
27. T, Otsuji, M. Hanabe, and O. Ogawara, "Terahertz plasma wave resonance of two-dimensional electrons in InGaP/InGaAs/GaAs high-electron-mobility transistors," Appl. Phys. Lett. **85**, 2119-2121 (2004).
28. F. Teppe, D. Veksler, V. Yu. Kachorovski, A. P. Dmitriev, X. Xie, X.-C. Xhang, S. Rumyantsev, W. Knap, and M. Shur, "Plasma wave resonant detection of femtosecond pulsed terahertz radiation by a nanometer field-effect transistor," Appl. Phys. Lett. **87**, 022102 (2005).
29. M. Hanabe, T. Otsuji, T. Ishibashi, T. Uno, and V. Ryzhii, "Modulation effects of photocarriers on the terahertz plasma-wave resonance in high-electron-mobility transistors under interband photoexcitation," Jpn. J. Appl. Phys. **44**, 3842-3847 (2005).
30. M. Lee, M. C. Wanke, and J. L. Reno, "Millimeter wave mixing using plasmon and bolometric response in a double-quantum-well field-effect transistor," Appl. Phys. Lett. **86**, 033501 (2005).
31. S. J. Smith and E. M. Purcell, "Visible light from localized surface charges moving across a grating," Phys. Rev. **92**, 1069 (1953).
32. K. S. Yee, "Numerical solution of initial boundary value problems involving Maxwell's equations in isotropic media," IEEE Trans. Antennas Propag. **AP-14**, 302-307 (1966).
33. R. J. Luebbers, F. Hunsberger, and K. S. Kunz, "A frequency-dependent finite-difference time-domain formulation for transient propagation in plasma," IEEE Trans. Antennas Propag. **39**, 29-34 (1991).
34. P. G. Huggard, J. A. Cluff, G. P. Moore, C. J. Shaw, S. R. Andrews, S. R. Keiding, E. H. Keiding, E. H. Linfield, and D. A. Ritchie, "Drude conductivity of highly doped GaAs at terahertz frequencies," J. Appl. Phys. **87**, 2382-2385 (2000).
35. J. A. Porto, F. J. Garchia-Vidal, and J. B. Pendry, "Transmission resonances on metallic gratings with very narrow slits," Phys. Rev. Lett. **83**, 2845-2848 (1999).
36. Y. Takanashi, K. Takahata, and Y. Muramoto, "Characteristics of InAlAs/InGaAs high-electron-mobility transistors under illumination with modulated light," IEEE Trans. Electron Devices **46**, 2271-2277 (1999).
37. H. Ito, S. Kodama, Y. Muramoto, T. Furuta, T. Nagatsuma, and T. Ishibashi, "High-speed and high-output InP–InGaAs unitraveling-carrier photodiodes," IEEE J. Sel. Top. Quantum Electron. **10**, 709-727 (2004).
38. S. Verghese, K. A. McIntosh, and E. R. Brown, "Highly tunable fiber-coupled photomixers with coherent terahertz output power," IEEE Trans. Microwave Theory Tech. **45**, 1301-1309 (1997).

1. Introduction

Specific features of two-dimensional (2D) plasmons in a submicron high-electron mobility transistor (HEMT) promote resonant oscillations in the terahertz range, which is expected to realize frequency-tunable oscillators/detectors as well as frequency multiplier functions for terahertz electromagnetic waves [1, 2]. When the carrier density becomes very high, the electron system behaves as plasma fluid. The electron channel acts as a plasmon cavity; its resonant frequency is determined by the gate length and the plasmon velocity. When one assumes a 100-nm gate length and compound semiconductors like GaAs of InP based material systems, the resonant frequency falls in the terahertz range. What is important is the plasmon velocity is proportional to the square root of the electron density which is controlled by the gate bias, giving rise to the tunability on resonant frequency. This results in a possibility of injection-locked frequency-tunable oscillation, which is essential for the applications to the synchronized operation of communications networks and/or measurement systems. So far, various analytical [1-13] and experimental studies [14-30] on the plasma-wave resonance in HEMT's or similar field-effect transistors (FET's) have been reported. Plasmon resonances and/or related electromagnetic emissions in the terahertz/sub-terahertz range have been reported by several groups.

Laser two-photon irradiation can make plasmon resonant excitation at the difference terahertz frequency so that the device can act as a terahertz photomixer [9,12]. So far, various studies on the terahertz plasma-wave photomixers have been reported [9,11-13,21,24,27,29]. 2D plasmon itself is a non-radiative mode so that a mean of mode conversion must be accompanied to yield efficient terahertz electromagnetic-wave emission. A metal-wired grating structure is frequently utilized for that purpose [6,11,14-17,19,23,30], which is well known as the Smith-Purcell effect [31]. Several unique structures including double-heterostructures [23,30] or doubly-interdigitated gratings [16] as well as log-spiral antenna with interdigital electrodes [11] have been reported to enhance the conversion gain. Those proposals, however, would be insufficient to realizing room-temperature operation. In this paper we propose a novel terahertz plasma-wave photomixer that effectively improves the conversion gain and terahertz radiation power. Its nonlinear field emission properties against structure-dependent characteristic parameters are numerically analyzed.

2. Device

2.1. Device structure and operation

Figure 1 illustrates the cross section of the newly proposed terahertz photomixer. The device structure is based on a high-electron mobility transistor (HEMT) and incorporates (a) doubly interdigitated grating gates (G1 and G2) that periodically localize the 2D plasmon in 100-nm regions with a micron interval and (b) a vertical cavity structure in between the top grating plane and a terahertz mirror at the backside. The terahertz mirror is a transparent metal like indium titanium oxide (ITO) making the plasmon excitation by optical two-photon irradiation from outside the back surface. (a) works as a terahertz antenna and (b) works as an amplifier. The cladding guide with a low ε is an option for better confinement of the vertical cavity.

When co-lineally polarized two CW laser beams having slightly different frequencies (f_0 and $f_0 + \Delta f$) are absorbed in the 2D electron channel, photoexcited carriers [12] and/or phonon-polariton modes [9] can coherently excite the periodically localized 2D plasmon at the difference frequency Δf so that it makes a photomixing function. If the excitation frequency matches to the standing wave condition of the localized 2D plasmon, the 2D plasmon makes resonant oscillation. The plasma wave itself is a non-radiative mode. The periodically localized 2D plasmon, however, can be coupled with those in neighbor regions and make in-phase resonant oscillation so that the 2D-plasmon grating can convert the non-radiative plasma waves to radiative electromagnetic waves. One unique feature is the mode conversion gain produced by another grating coupler: the doubly interdigitated gate strips, whose performance will be discussed in detail later.
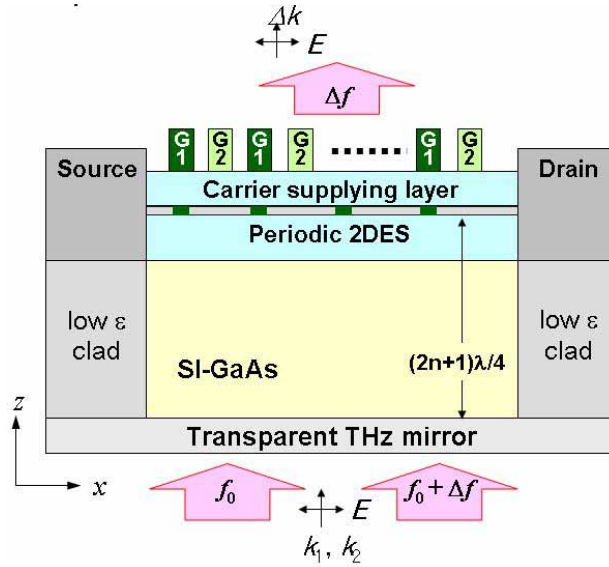
Fig. 1. Device cross section. The bottom terahertz mirror is transparent to the optical signals. k_1 and k_2: the wave vectors of irradiated photons, E: the electric field (linear polarization), Δk: the wave vector of electromagnetic radiation. 2DES: two dimensional electron systems.

Once the terahertz electromagnetic waves are produced from the seed of plasma waves, downward-propagating electromagnetic waves are reflected at the mirror back to the plasmon region so that the reflected waves can directly excite the plasmon again via intersubband transition process [18]. When the plasmon resonant frequency satisfies the standing-wave condition of the vertical cavity, the terahertz electromagnetic radiation will reinforce the plasmon resonance in a recursive manner according to the Drude-optical conductivity. Therefore, the vertical cavity may work as an amplifier if the gain exceeds the cavity loss.

2.2. Characteristic parameters

Field emission properties of the photomixer are characterized by the structure dependent key parameters shown in Fig. 2. The primary parameter that initiates the plasmon resonance is ω_{p2} which is the plasma frequency, i.e. plasmon characteristic frequency, of the periodically confined *gated* plasmon cavities. Each cavity is connected by the connecting portion whose carrier density must be controlled to be far apart from that in the plasmon cavity to make a good plasmon confinement. Thus, this connecting portion has its characteristic frequency ω_{p3}. The grating gate has also its own plasma frequency ω_{p1}. Note that ω_{p2} and ω_{p3} for the *gated* plasmon cavities and connecting portions obey the linear dispersion law while ω_{p1} for the *ungated* gate gratings is proportional to the square-root of wave vector [1, 2, 6]. All the three parameters are mainly determined by their cavity length: W, the distance between layers: d,
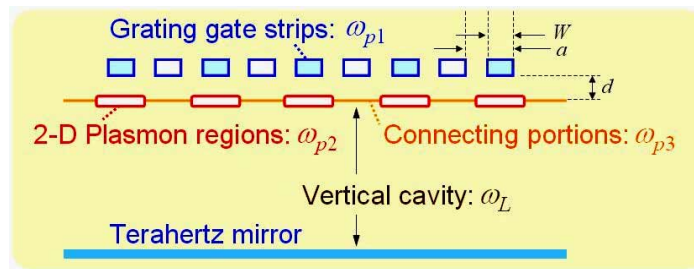

Fig. 2. Characteristic frequencies.

and carrier density, and perturbed by their periodicity: a, or the filling parameter: $f = W/a$ [6]. The final parameter, denoted by ω_L, corresponds to the vertical cavity resonance.

According to the operating frequency band, the grating geometry (single plasmon cavity length and periodicity) is designed to be fixed and ω_{p1} ω_{p3} as well as ω_L are optimally designed. For an actual device operation, ω_{p2} is a given parameter, which is first tuned by the gate bias at a specific value to obtain a desired resonance frequency. As a fundamental design criterion to obtaining high quantum efficiency, ω_{p1} and ω_L values are to be matched to ω_{p2} value while ω_{p3} is far depart from them. Once the device dimensions and material systems are designed, ω_{p1} and ω_L become fixed parameters. ω_{p3} for the connecting portion, on the other hand, is controllable (by V_{g2}) so that one can set it at far higher or lower than ω_{p2} by making the connecting portion to be metallic or dielectric.

3. Analysis

3.1. FDTD simulation

Figure 3 depicts the simulation flowchart. Two-photon excitation P_{in} (W) is the initial trigger to excite the plasmon. Then the plasmon excitation U_{aIB} is modeled as $\eta_{IB} P_{in}$, where η_{IB} the excitation efficiency. The plasma wave behavior of the 2D electron systems (2DES) is described by the extended Dyakonov-Shur model [1, 5]. Under the gradual channel approximation, the local density n and velocity v of the plasma fluid are formulated by the hydrodynamic equations:

$$m_e\left(\frac{\partial \boldsymbol{v}}{\partial t} + (\boldsymbol{v}\cdot\nabla)\boldsymbol{v}\right) = -e\nabla U - m_e \frac{\boldsymbol{v}}{\tau}, \tag{1}$$

$$\frac{\partial n}{\partial t} + \nabla(n\boldsymbol{v}) = \frac{\partial U}{\partial t} + \nabla(U\boldsymbol{v}) = 0, \tag{2}$$

where m_e the electron effective mass, e the electronic charge, U the gate-to-channel potential, τ the plasmon relaxation time. Their time-evolved response to the terahertz excitation was numerically analyzed using the finite differential time-domain (FDTD) method [32]. The
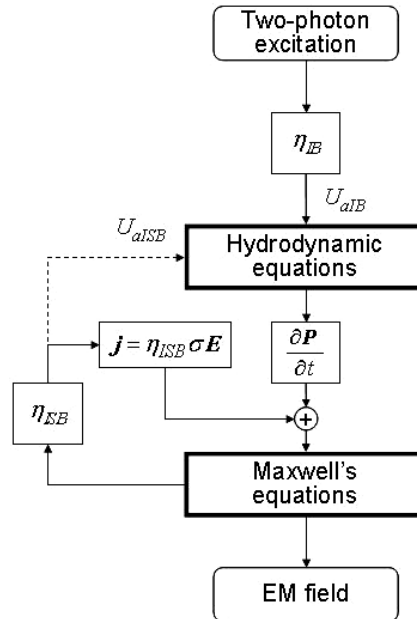

Fig. 3. Simulation flowchart.

plasma waves themselves are the coherent electronic polarization so that they should produce local displacement AC current. Thus, it was input to the Maxwell's FDTD simulator as a current source to analyze the electromagnetic field dynamics.

According to the standard Yee algorithm [32], Maxwell's equations are differentiated in the time-space dimension. The Drude-optical conductivity and permittivity [34] were modeled by a recursive convolution method [33]. The series of the FDTD simulation reveals the temporal response of the photomixer, i.e. terahertz electromagnetic radiation from the 2D plasmon excitation. It is noted that in the Maxwell's simulation the damping factors of plasmon-induced electromagnetic wave motions are expressed as the Drude conductivities of the plasmon cavities (σ_2) and the connecting portions (σ_3). Thus these two parameters as well as τ in the hydrodynamic simulation are very important to numerically calculate the total field emission efficiency, which will be discussed later.

The downward-propagating terahertz electromagnetic waves are reflected at the terahertz mirror back to the plasmon cavity grating and excite the plasmon via inter-subband absorption. Its plasmon excitation efficiency is denoted with η_{ISB} in Fig. 3. This plasmon re-excitation process is a non-linear phenomenon so that it should be simulated by the hydrodynamic simulator self-consistently (shown with a dashed arrow with an excitation U_{aISB} in Fig. 3). However, since its nonlinear effect is weak and the harmonic components only affect the field dynamics as weak perturbation, the excitation was linearized as shown in Fig. 3 with a solid line. η_{IB} and η_{ISB} are the key parameters to determine absolute radiation power as well as mode conversion gain. Since those exact values depend on the material systems, however, at first they are assumed to be 1.0×10^{-1} from a simple estimation as the product of the quantum efficiency and the absorption rate for relativistic discussion on field emission spectra, and then quantitatively discussed in the topics of maximum available output power.

3.2. Device model

Figure 4 shows a virtual structure and typical parameters for simulation. InGaP/InGaAs heterostructure material systems on a 8-μm thick SI-GaAs substrate and room-temperature operation were assumed. The electron channel acting as a plasmonic cavity grating is formed with a 50-nm thick InGaAs layer sandwiched with an upper 60-nm thick InGaP carrier supplying layer and a lower 500-nm thick GaAs buffer layer. Because of the limited memory space, nine periods of grating structures were modeled. The density of 2DES was periodically set as a pair of connecting and plasmon cavity region corresponding to the gate gratings G1 and G2, respectively. In the hydrodynamic simulation, τ was set at 10^{-12} sec. The nominal conditions of the density of electrons n_2 (n_3) and conductivity σ_2 (σ_3) for the plasmon cavity (connecting) region are 1.0×10^{12} cm^{-2} (1.1×10^6 cm^{-2}) and 88,000 S/m (0.1 S/m),
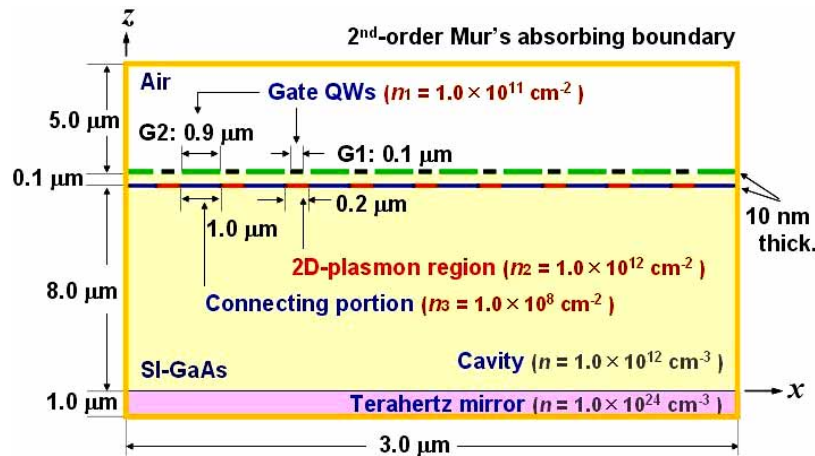

Fig. 4. Device model for numerical simulation. QW: quantum wire.

respectively. The length of the plasmon cavity and connecting portion are set at 200 nm and 1.0 μm, respectively, which gives the fundamental plasma frequency ω_{p2} of 3.4 THz under the nominal n_2 condition. The doubly interdigitated gate strips are assumed to be quantum wires [6] placed on top of the channel in a 100-nm distance whose nominal conductivity was set at a slightly lower ($n_1 = 4.0 \times 10^{11}$ cm^{-2}) level so as to roughly coincide the plasma frequency ω_{p1} with ω_{p2}. The thickness of the 2DES and the quantum wired gate gratings were assumed to be the numerical lattice constant of 10 nm. The vertical cavity length was set at the quarter wavelength of ω_{p2} so that ω_L be 3.4 THz. For each simulation, n_2 value was appropriately set so as to make ω_{p2} value coincide with the excitation frequency. The bottom surface was set either as the perfect electric boundary condition or as the absorptive boundary condition without the mirror (for comparison). All the other outer surfaces were treated as the second-order Mur's absorbing boundary.

3.3. Results

Figure 5 shows typical instantaneous cross-sectional distribution of the electric-field intensity along the x direction under a constant sinusoidal plasmon excitation at (a) a tuned frequency of 3.4 THz and (b) a detuned frequency of 5.1 THz. The characteristic frequencies ω_{p1} and ω_L were set at 3.4 THz. The primary parameter ω_{p2} were set at the excitation frequency (3.4 THz for (a) and 5.1 THz for (b)). All the plasmon cavities were excited in phase. One can see the standing wave oscillation inside the cavity and forward propagating quasi-transverse electromagnetic (TEM) waves outside in air. Small diffractions are seen for electromagnetic
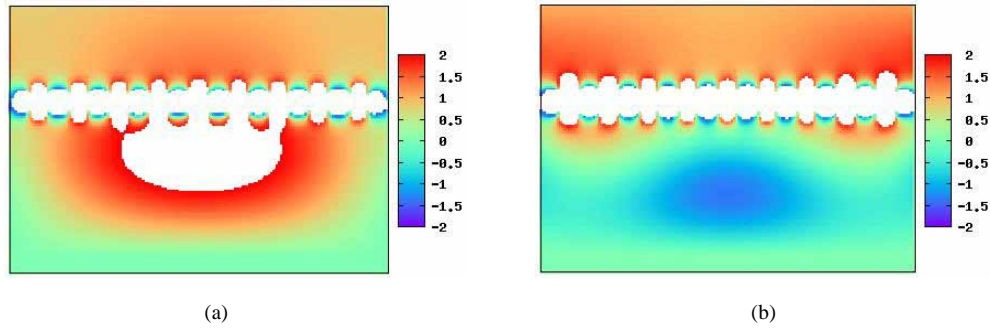

(a)   (b)

Fig. 5. Movies of simulated instantaneous electric field (E_x) distributions under a constant sinusoidal plasmon excitation (a) at 3.4 THz (732 KB) and (b) 5.1 THz (748 KB). Intensity scaled on the indicator is in arbitrary unit.
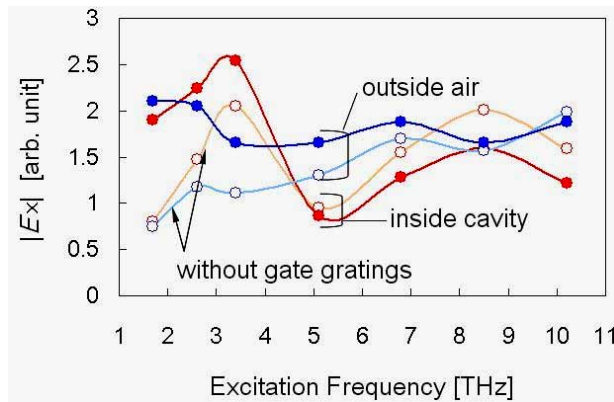

Fig. 6. Simulated electric field intensity (x component) vs. plasmon excitation frequency.

propagation near the source and drain side-edges, but an actual device having a large number of gate fingers may reduce such disturbance. The white colored area shows very high intensity of over the range. So the intensity is gaining time by time. The plasmon energy is satisfactorily converted to the electromagnetic radiation along the z direction. One can see in Fig. 5(a) an inphase oscillation between outside air and inside the cavity since the vertical cavity length is set at the quarter wavelength of the fundamental mode. Under a detuned condition of 5.1-THz excitation, on the other hand, antiphase oscillation is seen as is expected. The radiation power is almost remained at the level of that for the tuned condition.

According to the same manner, the field emission intensity was calculated for various excitation frequencies to examine the frequency tunability of proposed photomixer. The primary parameter ω_{p2} were set at each excitation frequency. For comparison, we prepared for artificial structures without double gate grating. Figure 6 shows the electric field intensity $|Ex|$ versus excitation frequency measured at the central two points (4 μm beyond the gate surface (outside the air) and 4μm under the plasmon surface (inside the vertical cavity)). The vertical cavity resonant condition gives the peak intensity at 3.4THz inside the cavity but is less sensitive outside the air, resulting in a broadband radiation property. The result also indicates that the double grating coupler enhances the radiation power leading to the mode conversion gain in a relatively wide frequency range.

In order to examine how the double gate grating and vertical cavity structures contribute to the field emission properties, artificial structures without double gate grating and/or terahertz mirror are prepared for, and compared their impulse responses to that of original structure by using Maxwell's FDTD simulator. All the characteristic parameters were fixed at the nominal values ($\omega_{p1}= \omega_{p2}= \omega_{L}$=3.4 THz). Each plasmon cavity was excited with an impulsive current source simultaneously. Simulated temporal responses of the electric field (x component) at the central two points (4 μm beyond the gate surface and 4 μm beneath the plasmon surface) were Fourier transformed to obtain entire frequency spectra. Figure 7 plots the results. For the structures without gate gratings, neither *gated* plasmon modes nor the Smith-Purcell effect is produced resulting in no obvious field enhancement over the frequency range; a small dip below 1THz is an unphysical error caused in numerical process. The vertical cavity makes a resonance property and weakly enhances the radiation in narrow bands around the fundamental and second harmonic frequencies.
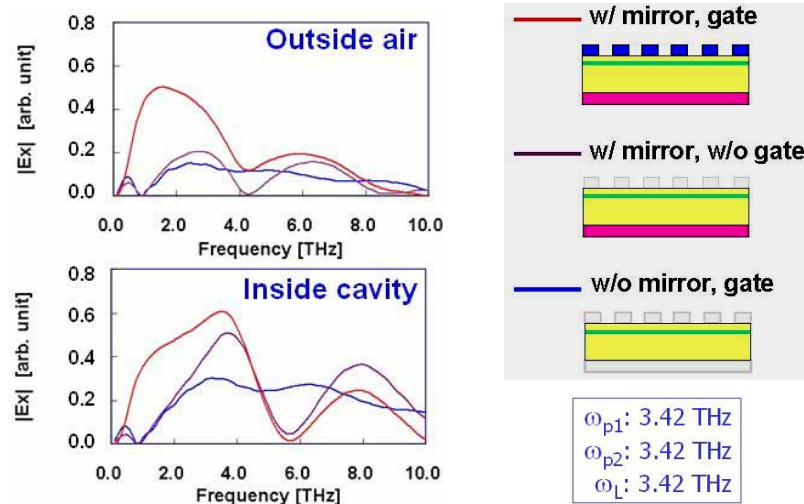

Fig. 7. Frequency responses for three different device structures to impulsive excitation at all the plasmon cavities. Electric fields (*x* component) at two points (inside the cavity and outside air) were calculated by using a Maxwell's FDTD simulator and their temporal profiles were Fourier transformed.

Incorporating the double gate grating, on the contrary, produces extraordinary electromagnetic transmission; the electric field intensity drastically enhances over a broadband range. As a result, mode-conversion gain, from non-radiative plasmon mode to radiative mode, of up to 14dB (a factor of 5) was successfully obtained in a wide frequency range from 600 GHz to 4 THz corresponding to the fundamental plasmon resonance. One can see the fundamental peak stays at around 1.8 THz outside the air, which is fairly lower than the original characteristic frequency of ω_{p2}. One possibility for this cause would be the excitation of vertically coupled surface plasmon polaritons as is seen in the interfaces of metallic gratings [35]. It is noted that the wavelength under consideration is by two orders of magnitude larger than the feature size of the grating, which is thought to be a consequence of excitation of complex plasmon modes produced in the grating-bicoupled unique structure.

3.4. Discussions

As is mentioned in *3.1*, the damping factors of plasmon-induced electromagnetic radiation are expressed as the Drude conductivities of the plasmon cavities (σ_2) and the connecting portions (σ_3) in the Maxwell's simulation. The sensitivity of the field emission intensity to σ_2 and σ_3 (equivalent to n_2 and n_3), therefore, should be considered. The Dyakonov-Shur model indicates that the plasmon resonant frequency ω_{p2} as well as its intensity is in proportion to the square root of σ_2. Moreover, the electromagnetic transmittance spectrum along through the grating-bicoupled device structure is attributed to the complex coupled modes among ω_{p1}, ω_{p2}, ω_{p3}, and ω_L. Since the total field emission properties are determined by the series connection of these responses as shown in Fig. 3, extensive mismatching between them may act as an excess nonlinear damping. On the other hand, as is mentioned in *2.2*, the parameter σ_3 must be far apart from σ_2 to obtain better plasmon confinement, which may affect the boundary condition at the plasmon cavity ends. Assuming a practical gate-bias modulation of the order of 1 V, however, fraction of σ_3 and σ_2 can easily be set at around two orders of magnitude, which may be less sensitive to the damping. Further discussion in detail will be published elsewhere in the near future.

Important questions are how broad the bandwidth is and how large the maximum available output power is. In this discussion, we consider the case of plasmon excitation by injecting real photoelectrons. First the bandwidth of photomixing is discussed. Since the plasmon resonance is a nature of electronic polarization, its entire bandwidth is given by the dielectric relaxation frequencies, and is well beyond 1 THz at a certain carrier density. In the sense of photoexcitation of plasmon resonance of our interest, therefore, the transport properties of photoexcited electrons injected to the 2D-plasmon cavity may limit the bandwidth.

When the incident optical electric field is $V(t) \propto (1 + m\cos\omega_m t)e^{i\nu t}$, where m the photomixing modulation index, ω_m the modulation frequency, and ν the optical frequency ($\omega_m \ll \nu$), the photo-injected current $i_{ph}(t)$ is expressed as

$$i_{ph}(t) = \frac{Pe\eta_{IB}}{h\nu}\left[(1 + \frac{m^2}{2}) + 2m \cdot \frac{1 - e^{-i\omega_m \tau_d}}{i\omega_m \tau_d} \cdot e^{i\omega_m t}\right], \qquad (3)$$

where P the optical incident power, e the electronic charge, h the Plank constant, η_{IB} the photon-electron quantum efficiency (due to interband photoexcitation), and τ_d the photoelectron transit time. The second term is the *ac* component, where $\omega_m \tau_m \approx 2.8$ gives the -3-dB bandwidth. Assuming practical values for d of 10 nm and a "hot" electron drift velocity of 2×10^7 cm/s, τ_d becomes 50 fs, resulting in a 3-dB bandwidth of 8.9 THz. If one will take virtual carrier excitation like phonon-polariton modes, the modulation will be free from the transit-time effect and the bandwidth exceeds well beyond 10 THz at the sacrifice of excitation efficiency by orders of magnitude.

Next, the maximum available output power and its saturation are examined. In case of plasmon excitation by means of injection of photoelectrons, the excitation efficiency is defined by the plasmon modulation index δ_{pm}: the ratio of the injected photoelectron density over the 2D electron density [29]. Since generation of photoelectrons has its own saturation property owing to the space-charge effect and the photovoltaic effect [36], the excitation efficiency saturates at a certain level and strongly depends on bias conditions. According to the photoresponse measurements for a standard HEMT device reported in [27, 29], δ_{ph} of up to 10% would be practical for an appropriate 2D plasmon density of 10^{12} cm^{-2}, resulting in a saturation photoelectron density $n_{ph\text{-}sat}$ of 10^{11} cm^{-2}. Assuming a photoelectron life time τ_{ph} of 1 ps, the saturation incident power density $P_{in\text{-}sat}$ becomes

$$P_{in-sat} = \frac{n_{ph-sat}h\nu}{\eta_{IB}\tau_{ph}} \approx O[10 \text{ kW/cm}^2].$$

(4)

Electrostatic calculation based on the drift-diffusion theory gives a drift velocity of the order of 10^7 cm/s for injection of photoelectrons, giving rise to a plasmon-induced saturation current density $j_{p\text{-}sat}$:

$$j_{p-sat} = en_{ph-sat}v_d = 0.16 \text{ [A/cm]}.$$

(5)

The open-loop maximum-available electromagnetic radiation power $P_{out\text{-}sat}$ (excluding re-excitation process showing as a feedback in Fig. 3) is estimated as

$$P_{out-sat} \approx G \cdot Z_{air} \cdot j_{p-sat}^2 \approx O[10 \text{ W/cm}^2],$$

(6)

where G the antenna gain factor (≈ 1.5), Z_{air} the free-space impedance $(\approx 377 \text{ }\Omega)$. As a consequence, the total open-loop conversion efficiency becomes $P_{out-sat}/P_{in-sat} \approx 10^{-3}$, which is higher by two to three orders of magnitude than those for conventional integrated photomixer devices such as UTC-PDs [37] and/or LT-GaAs photoconductors [38]. Assuming a typical dimension for a single photomixer device having 25 fingers of 100-nm-by-20-μm plasmon cavities, maximum available output power would be 7 μW with an incident optical power of 5 mW.

Moreover, the plasmon-amplitude stimulated-emission mechanism incorporated in the vertical cavity structure is expected to improve the efficiency and saturation. When we consider an actual η_{ISB} value corresponding to the feedback gain for non-radiative to radiative mode conversion, it is noted that the free carrier absorption of the bulk substrate material, not regarding in this work, may limit the conversion gain as well as broadband operation. We should choose appropriate material systems and their carrier densities according to the desired frequency range. Transferred substrate technique will be another option to cope with it.

4. Conclusions

We proposed a novel terahertz plasma-wave photomixer incorporating doubly interdigitated grating gates and resonant-enhanced vertical cavity structure. Frequency-dependent finite-differential time-domain analysis demonstrated that (i) grating-bicoupled plasmonic structure acts as a broadband terahertz photomixer and antenna and (ii) the vertical cavity structure effectively enhances the conversion gain and radiation power. The proposed device features various characteristic parameters of plasma frequencies some of which are electronically controllable so that it may provide broadband operation as well as design ease. The structure-sensitive design methodology for the device will be discussed in other publications. We are now evaluating the first test device, which will be also reported in other publications.

Acknowledgments